P4.25

ESTIMATION OF LAND SURFACE TEMPERATURE ON THE TIBETAN PLATEAU USING GMS DATA

Yuichiroh OKU, Hirohiko Ishikawa and Hiromasa Ueda
Disaster Prevention Research Institute, Kyoto University, Uji, Kyoto 611-0011, JAPAN

1. INTRODUCTION

The Tibetan Plateau has been thought to play an important role in the progress of Asian summer monsoon as an elevated heat source/sink protrudes into the middle of troposphere. To understand the interactions between the land surface and the atmosphere over the Tibetan Plateau in the context of the Asian monsoon system, an intensive meteorological observation was conducted in the GAME/Tibet (GEWEX Asian Monsoon Experiment) project (Koike et al., 1999). During the GAME/Tibet, surface sensible and latent heat fluxes were measured at some sites with eddy covariance technique together with the relevant monitoring of surface parameters such as land surface temperature, soil moisture, net radiation, surface albedo and others (Tsukamoto et al. 1999). Although the land surface atmosphere interaction is experimentally revealed at these sites, but they only represents fluxes in a patch scale around the measurement site. These patch scale information need to be integrated to regional information with the aid of satellite remote sensing. The surface measurements also revealed that the plateau boundary layer is characterized by its strong diurnal cycle (Tanaka et al. 2001). To detect the diurnal variation, the data observed by geostationary satellite should be used. For the Tibetan Plateau the GMS-5 provides continuous information of three infrared channels, two for split window (IR1, 11μm; IR2, 12μm) and one for water vapor channel (WV, 6.7μm).

We develop a methodology to retrieve one of important surface parameters, the land surface temperature, using GMS data. The retrieval algorithm originally developed for NOAA/AVHRR data has been applied to GMS-5 split-window measurements with some modification in this study. The general concept is shown in Fig. 1.

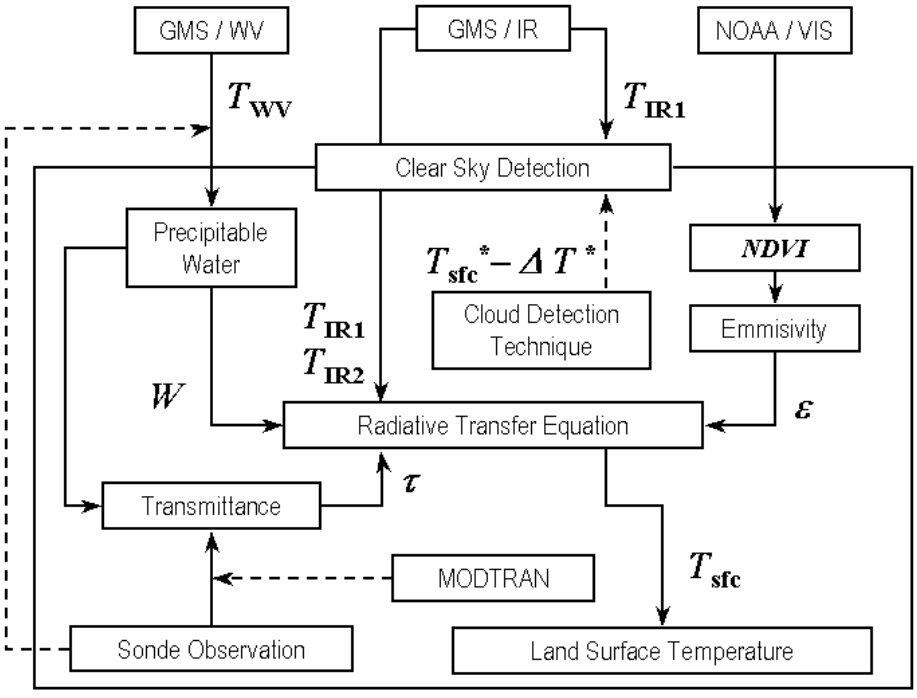

Fig. 1 Diagram of estimation land surface temperature procedure from the satellite data.

2. LAND SURFACE TEMPERATURE RETRIEVAL

The satellite remote sensing offers useful data to estimate regional distribution of various surface parameters. Algorithms of deriving surface temperature from the radiation data sensed by the earth observation satellites are proposed by many authors such as Wang et al. (1995), Bastiaanssen (1994) and others. Ma et al. (2001) retrieved surface temperature distribution over several 100 km scale on the Tibetan Plateau with the split-window technique using infrared brightness temperature of NOAA/AVHRR image. We applied the same algorithm for NOAA/AVHRR to GMS/VISSR data with necessary modification. It is applicable to GMS data, because the spectral of infrared sensor carried on GMS is similar to on NOAA (see Fig. 2).

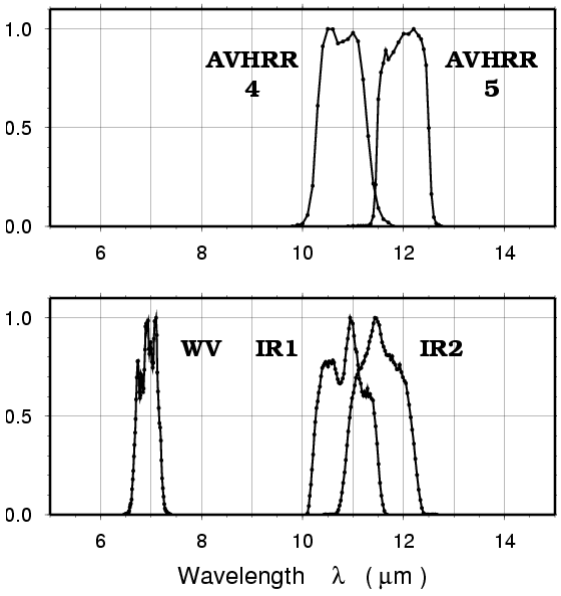

Fig. 2 Instrument response profile (normalized to a peak value of 1.0) as a function of wavelength λ of NOAA/AVHRR2 (upper) and GMS/VISSR (lower).

2.1 Data

GMS/VISSR image is continuously received at the Disaster Prevention Research Institute of Kyoto University. Surface temperature is calculated by the split-window technique modified for GMS using 11μm and 12μm brightness temperature. We first generated data referencing to longitude and latitude with 0.1-degree resolution interpolated from original image that is archived in the pixel-line format. The precipitable water required in the algorithm is retrieved from the water vapor channel (6.7μm), so the data are also arranged to the same grid. NOAA/AVHRR image, collected from NOAA Satellite Active Archive WWW site, are also converted to the 0.1-degree latitude-longitude grid, and are used to estimate surface emmisivity.

To adjust the algorithm to GMS, radiative transfer is calculated using MODTRAN. The atmospheric vertical profiles on the plateau required to run MODTRAN are taken from rawinsonde observations at Amdo during GAME/Tibet intensive observation period (IOP), from June to August 1998. The Chinese sonde data at various sites over the plateau are also utilized to confirm this precipitable water retrieval algorithm using GMS 6.7μm brightness temperature, which is tuned for Amdo data.

The surface temperature data observed by IR thermometer at Automatic Weather Stations (AWSs) in 1998 in D66, Tuotuohe, D110 and MS3608 are used for determination of threshold value of cloud detection. The surface observation data including these 4 AWS sites are utilized to compare with estimated surface temperature from satellite. The location of observation point is shown in Fig 3.

2.2 Algorithm

For cloud-free atmosphere under local thermodynamic equilibrium, the radiative transfer equation gives the radiance $I_{\nu\theta}$ measured from space by a satellite in wavelength ν with a zenith angle θ, and is expressed as

$$\begin{aligned} I_{\nu\theta} &= B_\nu(T_{\nu\theta}) \\ &= \varepsilon_{\nu\theta} B_\nu(T_{\mathrm{sfc}}) \tau_{\nu\theta} + R^{\uparrow}_{\mathrm{atm}\theta} + R_{\mathrm{ref}} \tau_{\nu\theta} \end{aligned} \quad (1)$$

B_ν is Plank's function, $\tau_{\nu\theta}$ is brightness temperature, $\varepsilon_{\nu\theta}$ the ground surface emissivity, $B_\nu(T_{\mathrm{sfc}})$ the radiance which would be measured if the surface were a blackbody

with the surface temperature T_{sfc}. $\tau_{v\theta}$ is the total atmospheric path transmittance, $R^{\uparrow}_{\mathrm{atm}\theta}$ the atmospheric upwelling radiance, R_{ref} the reflected atmospheric radiance (Sobrino et al. 1996). To be more conveniences, radiance from the atmosphere is replaced by its

Observation Station Name	Location (Latitude, Longitude, Altitude)			Surface Observation	Sonde Observation
D66	33.5°N	93.8°E	4,600m	○*	
Tuotuohe	34.2°N	92.4°E	4,535m	○*	△
D110	32.7°N	91.9°E	5,070m	○*	
MS3608	31.2°N	91.8°E	4,610m	○*	
Amdo	32.2°N	91.6°E	4,700m	△	△**
MS3478	31.9°N	91.7°E	5,063m	△	
Shiquanhe	32.5°N	80.1°E	4,279m	○	△
Gaize	32.1°N	84.4°E	4,416m	○	△
Naqu	31.5°N	92.1°E	4,508m		△
Lhasa	29.7°N	91.1°E	3,650m		△
Dingri	28.6°N	87.1°E	4,300m		△
Yushu	33.0°N	97.0°E	3,682m		△
Darlag	33.8°N	99.7°E	3,968m		△
Qamdo	31.2°N	97.2°E	3,307m		△
Linzhi	29.6°N	94.5°E	3,007m		△

*Table 1 List of the surface observation points and observed period. Circle indicates data in 1998 is available. Triangle indicates data only GAME/Tibet IOP, from June to August in 1998, is available. *For estimating the threshold of cloud detection technique. **For calculating regression line to estimate precipitable water from 6.7μm brightness temperature.*

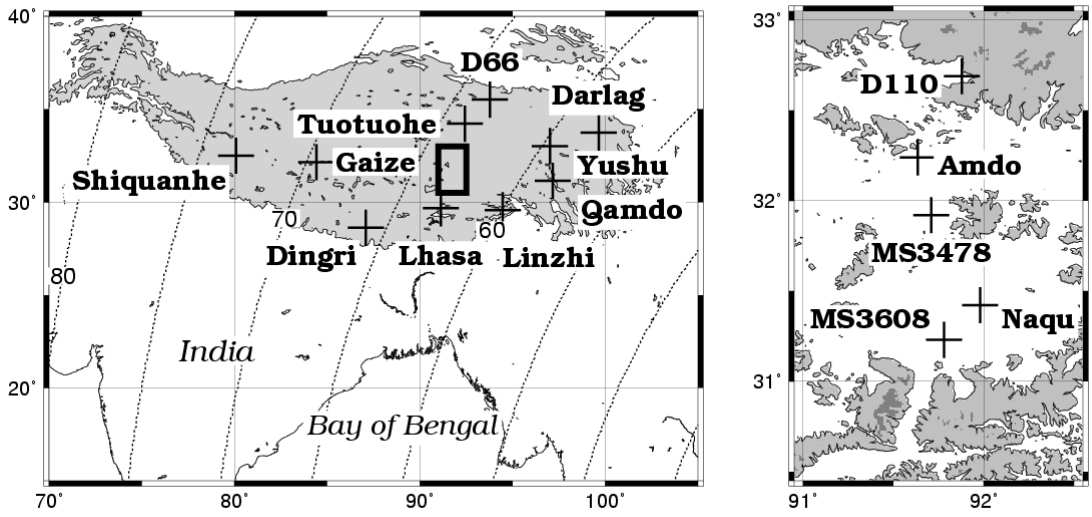

Fig. 3 Location of the observation point. Left panel also shows distribution of the satellite zenith angle from GMS with dot curve over the Tibetan Plateau. Contour interval is 5 degree. The shaded area in the left panel indicates altitude higher than 4,000m ASL and bold square is the enhanced observation area for GAME/Tibet, whose topography shows in the right panel. The light shaded area in the right panel indicates altitude greater than 4,500m ASL, the dark shaded area is also shown over 5,000m ASL.

temperature term, that is

$$R^{\uparrow}_{\mathrm{atm}\theta} = (1-\tau_{vi\theta})B_{\nu}(T_{\mathrm{air}}) \qquad (2)$$

In term of R_{ref}, for simplicity, we have assumed that the sky radiance is isotropic, down welling atmospheric radiance can be replaced by the radiance emitted by the atmosphere in the 53 degree direction, that is,

$$R_{\mathrm{ref}} = (1-\varepsilon_{v\theta})(1-\tau_{v53^{\circ}})B_{\nu}(T_{\mathrm{air}}) \qquad (3)$$

Equation (1) is applied to 11μm and 12μm, and rewritten as

$$B(T_{\mathrm{IR1}}) = \varepsilon_1 B(T_{\mathrm{sfc}})\tau_1 + \{(1-\tau_1) + (1-\varepsilon_1)(1-\tau_{53^{\circ}})\tau_1\}B(T_{1\mathrm{air}}) \qquad (4)$$

$$B(T_{\mathrm{IR2}}) = \varepsilon_2 B(T_{\mathrm{sfc}})\tau_2 + \{(1-\tau_2) + (1-\varepsilon_2)(1-\tau_{53^{\circ}})\tau_2\}B(T_{2\mathrm{air}}) \qquad (5)$$

Subscript 1 and 2 represent 11μm and 12μm channel respectively. τ_{53} is the transmittance at the zenith angle 53 degrees and T_{air} a mean temperature of atmosphere. Solving (4) and (5) yields a equation for T_{sfc},

$$T_{\mathrm{sfc}} = T_{\mathrm{IR1}} + A(T_{\mathrm{IR1}} - T_{\mathrm{IR2}}) - B - C(1-\varepsilon) - D\Delta\varepsilon \qquad (6)$$

where $\varepsilon = (\varepsilon_1 - \varepsilon_2)/2$ is the average emmisivity in both channels and $\Delta\varepsilon = (\varepsilon_1 - \varepsilon_2)$ the spectral variation of emissivity. A, B, C and D are the coefficients which are

$$A = \frac{1-\tau_1}{\tau_1 - \tau_2} \qquad (7)$$

$$B = A(1-\tau_2)(T_{1\mathrm{air}} - T_{2\mathrm{air}}) \qquad (8)$$

$$C = \frac{1-\tau_1\tau_{53^{\circ}}}{\tau_1 - \tau_2}(T_{\mathrm{IR1}} - T_{\mathrm{IR2}}) + \tau_{53^{\circ}}\frac{T_{\mathrm{IR1}}}{4.667} \qquad (9)$$

$$D = \tau_2 AC \qquad (10)$$

All τ and T_{air} are derived from the result of radiative transfer simulation with MODTRAN as a function of both precipitable water W and satellite zenith angle θ. For detail, see section 2.4.

2.3 Surface Emissivity

The surface emissivity depends on the surface characteristics such as the vegetation and the surface wetness, so that its diurnal variation is expected to be relatively small. Therefore, we estimated the surface emissivity from NOAA/AVHRR visible channels. The procedure is same as Sobrino et al. (2000), and is derived from Normalized Difference Vegetation Index (NDVI) calculated from NOAA visible channels.

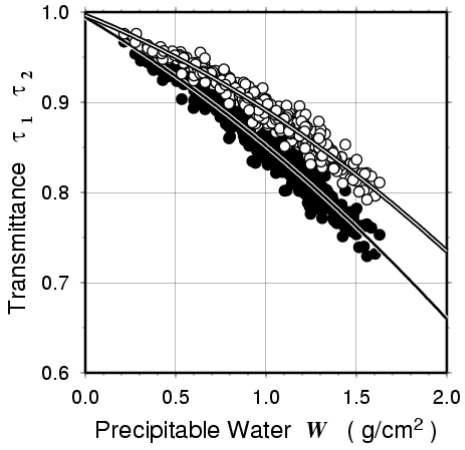

Fig.4 Atmospheric transmittance for GMS/VISSR 11μm band τ_1 (circle), and 12μm τ_2 (dot) with the regression curve as a function of the precipitable water.

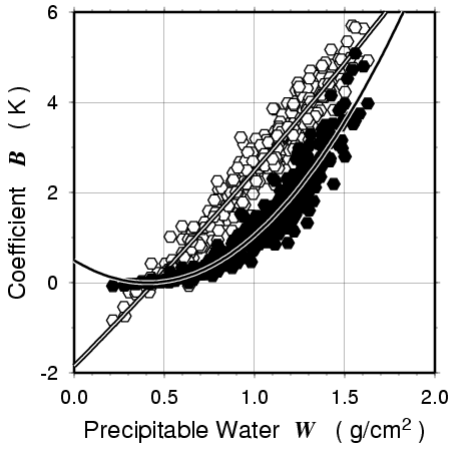

Fig.5 Atmospheric temperature difference between 11μm and 12μm $T_{1\mathrm{air}} - T_{2\mathrm{air}}$ (circle), and coefficient B (dot) culculated from equation (8) with the regression curve as a function of the precipitable water.

2.4 Coefficients

Both The atmospheric temperature and path transmittances depend on the vertical profile of gaseous compounds of atmosphere such as water vapor or carbonic anhydride. They cannot be derived directory from GMS or NOAA data. Many authors assume that fluctuation of atmospheric attenuation mainly depends on precipitable water which is integrated value of water vapor vertically, and they use radiative transfer model with various atmospheric profile to estimate atmospheric transmittances. In this study, similarly, the atmospheric transmittances are determined as a regression function of precipitable water using MODTRAN. The vertical profiles of pressure, temperature and relative humidity are given by radiosonde data observed over 300 cases during GAME/Tibet IOP in Amdo (91.63°N, 32.24°E). The profiles of gases except for water vapor were assumed as the typical value in mid-latitude built in MODTRAN. In addition to these atmospheric data, geographical and surface condition in Amdo, such as zenith angle from GMS, are put into MODTRAN. Some results, τ_1 and τ_2 are shown in Fig. 4. These cases are for satellite zenith angle 60 degree.

The term $T_{1\mathrm{air}} - T_{2\mathrm{air}}$ and coefficient B are shown as a function of precipitable water as same as transmittances in Fig. 5. From these results, transmittance and atmospheric temperature on the plateau are sensitive to the amount of precipitable water. Furthermore, satellite zenith angle in the western edge of the plateau is 20 degree larger than in the eastern edge. Distribution of the satellite zenith angle of GMS on the plateau is shown in Fig 1 by dotted lines. If satellite zenith angle at the target is larger, the atmospheric attenuation is expected to be greater. Therefore, these coefficients should be determined not only as functions of precipitable water but also as functions of sattelite zenith angle. So we calculated radiative transfer on the various satellite zenith angles, which vary from 50 degree to 75 degree. For each zenith angle regression curve was estimated, and finally coefficients A to D in equation (6) is derived as a function of both precipitable water and satellite zenith angle. Examples are shown in Fig 6 for coefficients A and B.

2.5 Presipitable Water

A strong relationship is found between 6.7μm brightness temperature T_{WV} and precipitable water W over the Tibetan Plateau, because the weighting function of 6.7μm is large around 400hPa level (Yatagai 2001). Fig. 7 shows the scatter diagram between 6.7μm brightness temperature of a pixel including Amdo and precipitable water calculated from radiosonde data at Amdo.

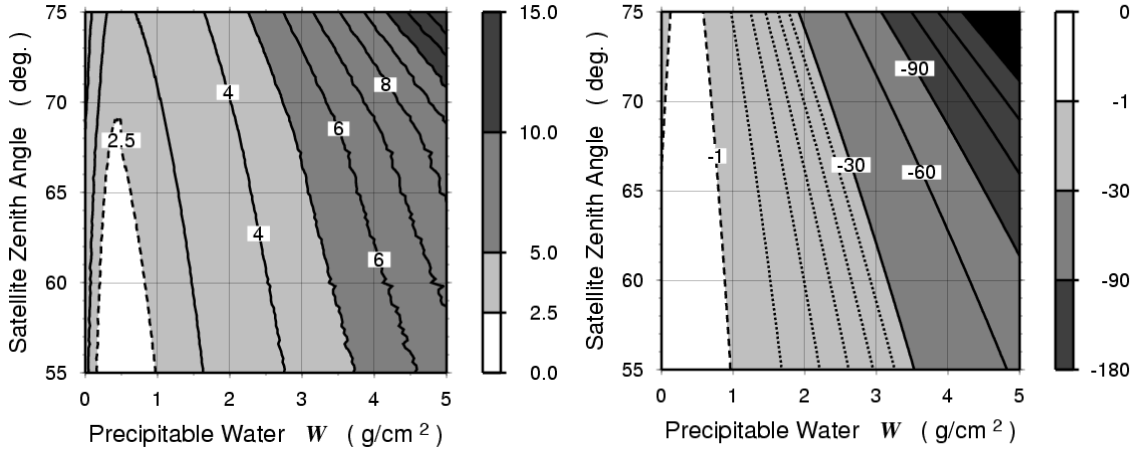

Fig.6 Distribution of the coefficients A (left panel) and B (right panel) calculated from equations (7) and (8), respectively, as a function of both the precipitable water W (horizontal axis) and satellite zenith angle θ from GMS (vertical axis). From each result of the radiative transfer simulation with MODTRAN, regression curve was estimated, and then the coefficients are derived.

Dots show clear sky cases and circles show cloudy cases, classified by the cloud detection technique (see chapter 3). Linier regression is calculated only for clear data, because the surface temperature can be estimated over cloud free area.

With this relationship, precipitable water over the plateau can be estimated from 6.7µm brightness temperature directly.

3. CLOUD REMOVAL

We cannot estimate land surface temperature over cloudy area, because equation (1) is only available when the satellite receive radiation from the surface, not from the cloud top. To derive land surface temperature accurately, it is essential to detect cloud-covered area correctly.

Cloud detection using visible channel data is relatively easy and accurate, but only available during daytime. Many authors utilize brightness temperature of infrared channel to detect convective clouds by threshold method. For example, Nitta and Sekine (1994) uses 250 K as the threshold value to detect convective clouds over the equator. Ueno (1997) uses 240 K over the Tibetan Plateau. But, according to Tanaka et al. (2001), in winter midnight the surface temperature observed on the plateau sometimes reaches less 240 K and its diurnal range over 30 K.

Fig. 8 indicates seasonal variation of the surface temperature observed by AWSs at 00 UT. Local solar time (LT) is 6 hours ahead of universal standard time (UT). Solid curve in this figure shows regression from composite data. Fig. 9 is an assemble of the regression curves as in Fig. 8 for each hour. It indicates that the observed surface temperature shows

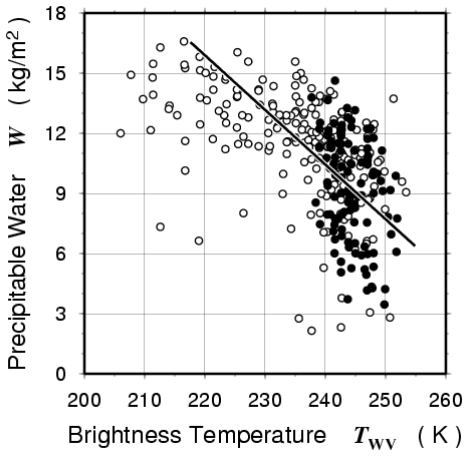

Fig.7 Scatter diagram of between 6.7µm brightness temperature T_{WV} (horizontal axis) and precipitable water W (vertical axis) calculated from sonde data. Dot indicates clear case and circle is cloudy case divided by using 11µm brightness temperature with cloud detection. Liner regression is indicated with a solid line.

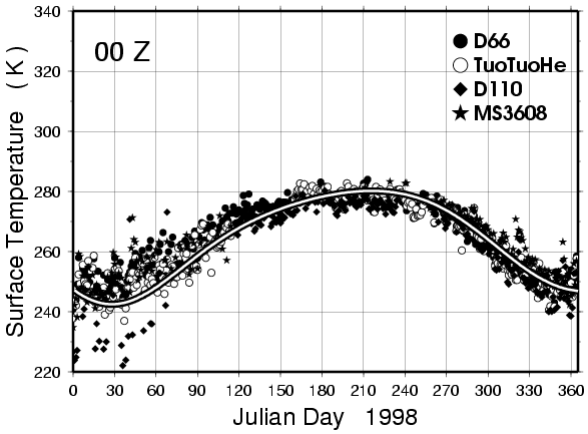

Fig.8 Seasonal variation of land surface temperature as a composite of 4 AWSs (D66, Tuotuohe, D110, MS3608) at 00 UT in 1998 observed by infrared radiation thermometer and its regression curve estimated using Fourier transform.

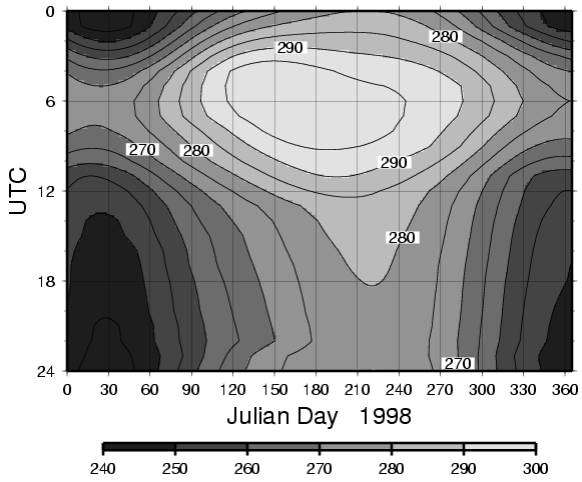

Fig.9 Seasonal (horizontal axis) and diurnal (vertical axis) variation of land surface temperature. Values obtained from the hourly regression curve, such as one indicated on Fig 8.

strong seasonal (horizontal axis) and diurnal (vertical axis) variation. Therefore the technique using fixed threshold value is enough to detect convective clouds, but is not sufficient to catch the radiation from the earth over cloud free area. In order to specify the surface correctly, it is necessary to adopt variable threshold adjusting to seasonal and diurnal variation of surface temperature. We assume that the scene is cloud free, if

$$T_{\mathrm{IR1}} < T_{\mathrm{sfc}}{}^{*} - \Delta T^{*} \qquad (11)$$

where $\Delta T_{\mathrm{sfc}}{}^{*}$ is a typical surface temperature shown in Fig. 9. ΔT^{*}=10K is adopted after various checking but are not mentioned here. The advantage of the present cloud detection scheme is illustrated in Fig. 10. The figure compares the GMS derived surface temperature with the field observation. The dots represent the present algorithm, the circles with fixed threshold algorithm, and the crosses the raw 11μm brightness temperature. It is clearly shown that the present algorithm detects the cloud free area appropriately.

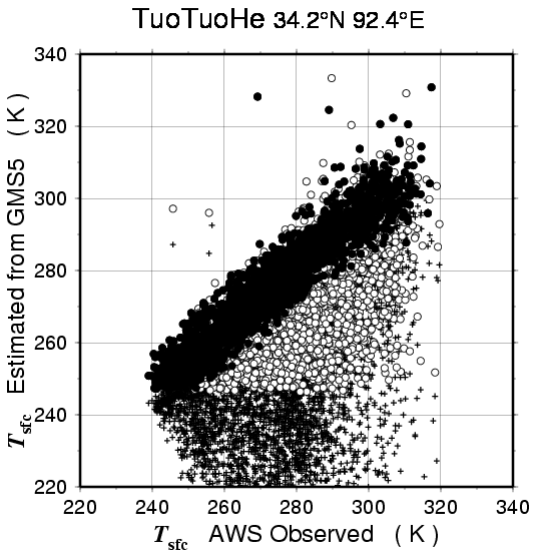

Fig.10 Scatter diagram between surface temperature observed by Tuotuohe-AWS (horizontal axis) and estimated from GMS with present cloud detection technique (dot, vertical axis), with fixed threshold technique (circle), and 11μm brightness temperature (cross).

4. RESULTS

We estimated surface temperature over the Tibetan Plateau in 1998 hourly. One of the results is shown in Fig. 11, from sunrise to daybreak, April 25,1998. In the morning, there are few clouds over the plateau, so surface temperature could be estimated nearly full area. The higher temperature over eastern area than western seems to be caused by sunrise.

To compare with zonal difference of surface temperature in pre-monsoon period, monthly averaged diurnal profile was calculated each domain, which is shown in Fig. 12. Diurnal range in the western plateau is larger than eastern, warmer in the daytime and colder in nighttime, and its difference reaches up to 5K. This result corresponds with Yanai and Li (1992), they found consideration sensible heating in the western plateau during pre-monsoon period. It should be considered that following. In the western plateau, it tends to dominant sensible heating rather than latent heating because of less wetness on the surface soil in pre-monsoon period. On the other hand, the eastern plateau relatively wet condition both lower atmosphere and surface than the western. So in the eastern that moisture condition reduces large diurnal range of surface temperature like in the western.

5. CONCLUSION AND REMARKS

We modified the algorithm to estimate surface temperature from satellite data for application to GMS, and calculated over the Tibetan Plateau in 1998. Also, new cloud detection technique with variable threshold that depends on both seasonal and diurnal is proposed instead of the fixed threshold method. The result indicates that it is possible to apply the algorithm to derive surface temperature for GMS. There is a problem about the resolution that caused GMS catches the radiation over the plateau with large angle. It is sufficient to analyze plateau scale distribution or variation with GMS data, but does not adequate to several 10km scale. To apply for the latter, it is necessary to utilize data produced by the satellite that has the sensor catches the radiation from the surface with small zenith angle, e.g. FY2b.

The largest advantage of utilizing GMS data is its high temporal resolution. The polar-orbit-satellite like NOAA provides only once or twice in a day, but we can get hourly data over the plateau scale from GMS. This advance makes it possible to analyze intra-diurnal variation over large area.

REFERENCES

Coll, C. and Caselles, V., 1997: A split-window algorithm for land surface temperature from advanced very high resolution radiometer data: Validation and algorithm comparison. *J. Geophys. Res.*, **102**, 16697-16713

Koike, T., Yasunari, T., Wang, J. and Yao, T., 1999, GAME-Tibet IOP Summary Report. *Proceeding of the 1st International Workshop on GAME-Tibet, Xi'an, China,* 1-2.

Ma, Y., 2001: Parameterization of land surface heat flux densities over inhomogeneous landscape combining satellite remote sensing with field observations. *Ph.D Thesis*

Nitta, T. and Sekine, S., 1994: Diurnal variation of convective activity over the tropical western pacific. *J. Meteor. Soc. Japan*, **72**, 627-641

Sobrino, J., A. and Li, Z.-L., Stoll, M. P. and Becker, F., 1994: Improvements in the split-window technique for land surface temperature determination. *IEEE Transactions on Geoscience and Remote Sensing*, **32**, 243-253

Sobrino, J., A. and Li, Z.-L., Stoll, M. P. and Becker, F., 1996: Multi-channel and multi-angle algorithms for estimating sea and land surface temperature with ATSR data. *Int. J. Remote Sensing*, **17**, 2089-2114

Sobrino, J., A. and Raissouni, 2000: Toward remote sensing methods for land cover dynamic monitoring: application to Morocco. *Int. J. Remote Sensing,* **21**, 353-366.

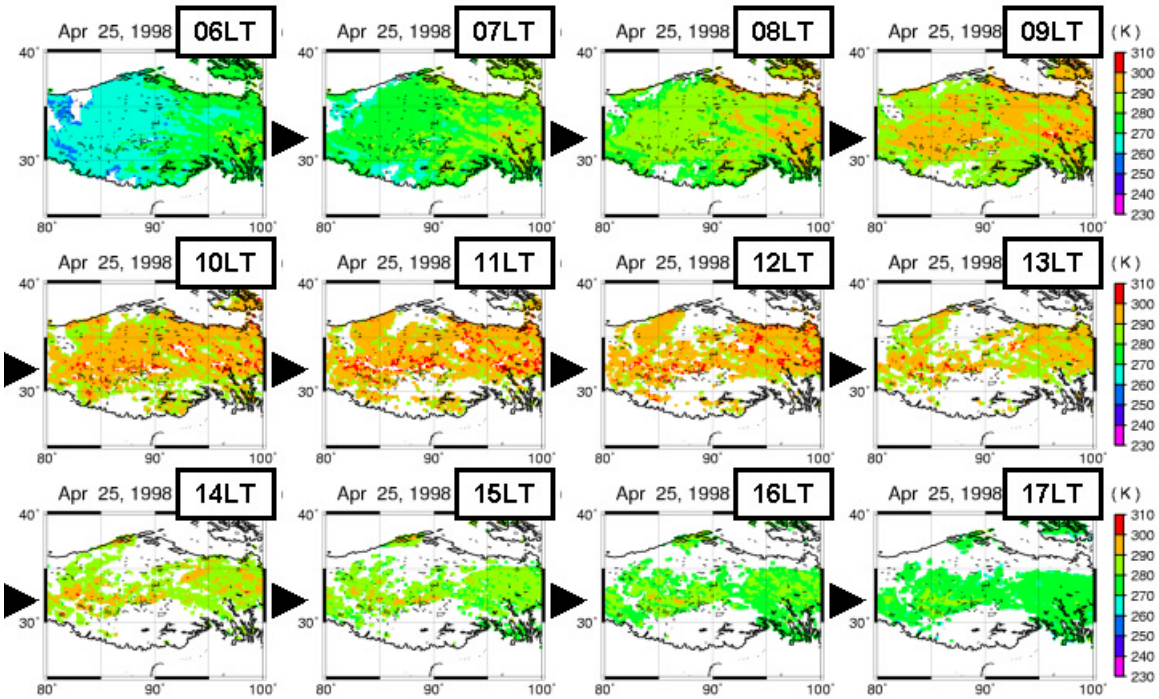

Fig.11 Hourly surface temperature estimated from GMS from 06LT (00UT) to 17LT (11UT), April 25, 1998. Local solar time is taken at 90°E. The area shaded with white over the Tibetan Plateau indicates cloudy.

Tanaka, K., Ishikawa, H., Hayashi, T., Tamagawa, I. and Ma, Y., 2001: Surface energy budget at Amdo on the Tibetan Plateau using GAME/Tibet IOP98 data. *J. Meteor. Soc. Japan*, **79**, 505-517.

Tsukamoto, O., Fudeyasu, H., Miyazaki, S., Ueno, K., Qi, Y., Ma, Y., and Ishikawa. H., 1999, Turbulent surface flux measurements over the Tibetan Plateau with flux-PAM system. *Proceeding of the 3rd international scientific conference on the global energy and water cycle workshop, Beijing, China,* 411-412.

Ueno, K., 1997: Some problems about the precipitation system in the Tibetan Plateau. *J. Geography*, **106(2)**, 293-301 (in Japanese).

Ueno, K., 1998: Characteristic of plateau-scale precipitation in Tibet estimated by satellite data during 1993 monsoon season. *J. Meteor. Soc. Japan*, **76**, 533-548.

Ueno, K., Fujii, H., Yamada, H. and Liu, L., 2001: Weak and frequent monsoon precipitation over the Tibetan Plateau. *J. Meteor. Soc. Japan*, **79**, 419-434.

Yatagai, A., 2001: Estimation of precipitable water and relative humidity over the Tibetan Plateau from GMS-5 water vapor channel data. *J. Meteor. Soc. Japan*, **79**, 589-598.

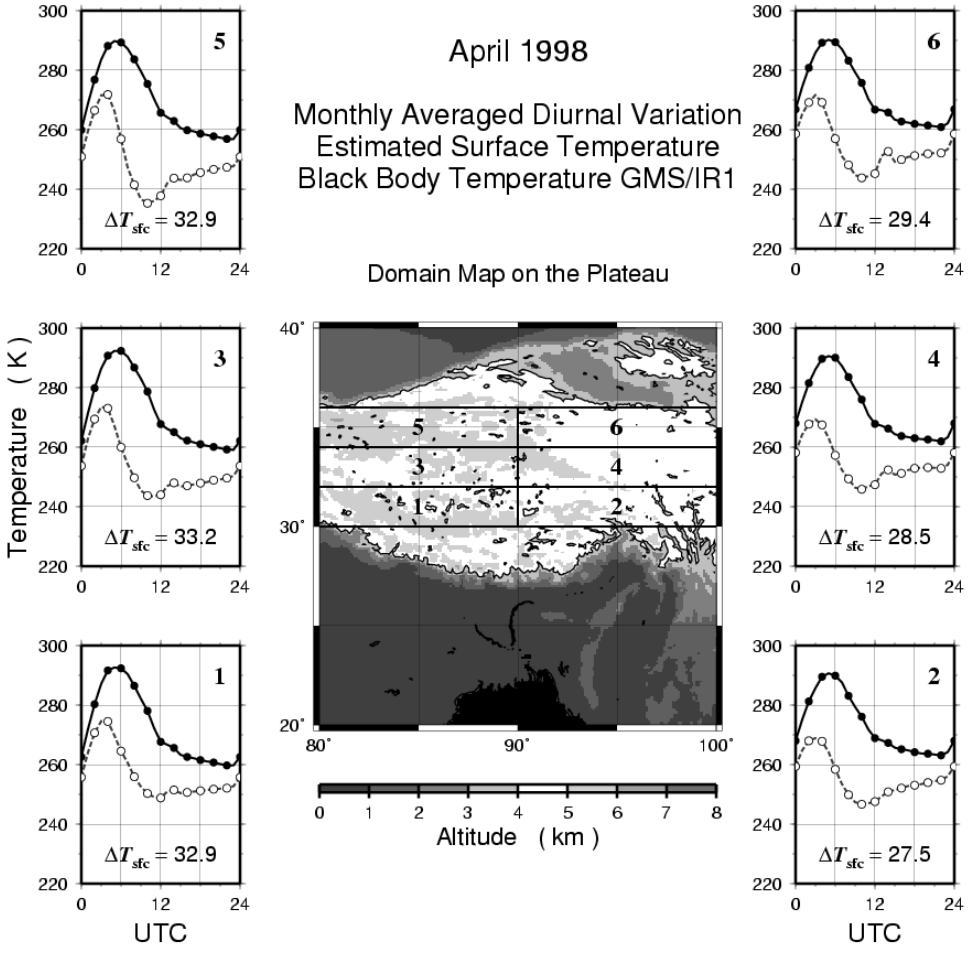

Fig.12 Monthly averaged diurnal variation of 11μm brightness temperature (circle, broken line) and surface temperature estimated from GMS (dot, solid line) in each domain over the Tibetan Plateau, in April 1998. Domain number indicated right upper in each graph refers to central topography map. Diurnal range of surface temperature each domain is shown lower in the graph as the value of ΔT_{sfc}.